



Sea Ice CCI+



ESA CCI+ CLIMATE CHANGE INITIATIVE
PHASE 1: NEW R&D ON CCI ECVs

Contract number:
4000126449/19/I-NB



CCI+ Sea Ice ECV SEA ICE CONCENTRATION ALGORITHM THEORETICAL BASIS DOCUMENT (ATBD)

Reference: D2.1

Issue: 3.1

Date: 10 August 2021



FMI



Max-Planck-Institut
für Meteorologie



 <p>Norwegian Meteorological Institute</p>	<p>The Norwegian Meteorological Institute (METNO) Henrik Mohns Plass 1 N-0313 Oslo Norway Phone: + 47 22 96 30 00 Fax: + 47 22 96 30 50 E-Mail: thomas.lavergne@met.no http://www.met.no</p>
--	---

<p>Contract PHASE 1 OF THE CCI+ CLIMATE CHANGE INITIATIVE NEW R&D ON CCI ECVs SEA ICE ECV</p>	<p>Deliverable D2.1 Sea Ice Concentration Algorithm Theoretical Basis Document</p>
<p>CLIENT European Space Agency</p>	<p>CLIENT REFERENCE 4000126449/19/I-NB</p>
<p>Revision date: 10 August 2021</p>	<p>Approval date: 27 September 2021</p>
<p>Principal Authors <i>Thomas Lavergne, Norwegian Meteorological Institute</i> <i>Atle M. Sørensen, Norwegian Meteorological Institute</i> <i>Rasmus Tonboe, Danish Meteorological Institute</i> <i>Leif Toudal Pedersen, Technical University of Denmark - DTU Space</i></p>	

Change Record

Issue	Date	Reason for Change	Author(s)
1.0	29.08.2019	First version	T. Lavergne, A. Sørensen, R. Tonboe
2.0	29.05.2020	Second version	T. Lavergne, R. Tonboe, A. Sørensen
2.1	22.06.2020	Minor updates addressing RIDs from ESA TO	T. Lavergne
3.0	30.06.2021	Third version	T. Lavergne, R. Tonboe, L. T. Pedersen
3.1	10.08.2021	Minor editorial revisions.	T. Lavergne

Document Approval

Role	Name	Signature
Written by:	T. Lavergne, A. Sørensen, R. Tonboe, L. T. Pedersen	
Edited by:	M. A. Killie	
Approved by:	A. M. Trofaier	

Contents

1 INTRODUCTION.....	6
1.1 Purpose.....	6
1.2 Scope.....	6
1.3 Document Status.....	6
1.4 Acronyms and Abbreviations.....	6
1.5 Executive Summary.....	8
2 HIGH(ER) RESOLUTION SIC USING THE NEAR-90 GHz IMAGERY (1991 - 2020)..	9
2.1 Complementarity and relation to EUMETSAT OSI SAF SIC data.....	9
2.2 Satellite and auxiliary data.....	10
2.3 The near-90 GHz linear (N90LIN) SIC algorithms.....	13
2.4 Resolution-enhanced reSICCI3LF SIC fields using pan-sharpening.....	17
2.5 Summary for the high(er) spatial resolution SICs using the near-90 GHz imagery channels.....	20
3 SEA ICE COVER WITH ESMR (1972 – 1977).....	22
3.1 Input and auxiliary data.....	22
3.2 Overview of the processing chain.....	24
3.3 Pre-processing of the data.....	25
3.4 Level-2 algorithms.....	26
3.5 Level-3 algorithms.....	29
3.6 Level-4 algorithms.....	30
4 STRATEGIES FOR AN IMPROVED 100% TIEPOINT DURING THE SUMMER MELT SEASON.....	31
4.1 Background.....	31
4.2 Detailed method description.....	34
4.3 Example results.....	35
4.4 Step by step procedure for improved Summer ice TPs.....	37
5 REFERENCES.....	38

1 INTRODUCTION

1.1 Purpose

This document is the Algorithm Theoretical Basis Document for the Sea Ice Concentration ECV product within CCI+ PHASE 1 - NEW R&D ON CCI ECVs. It documents the scientific background and algorithm details of the methodologies implemented to generate Sea Ice Concentration Climate Data Records.

1.2 Scope

The scope of the document is to describe elements of the algorithms that are deemed mature enough for implementation for the final production of the SIC CDRs, during the 3rd year of the CCI+ Phase 1 project. The selected algorithms are presented and justified, but the document does not hold results of the research work leading to the selection of these particular algorithms (some of this info is in D2.3 Update to ADP).

1.3 Document Status

This is the third version of the ATBD of the Sea Ice Concentration variable within CCI+ Phase 1. The first two versions were internal to the project (non-mature algorithms).

1.4 Acronyms and Abbreviations

The table below lists the acronyms and abbreviations used in this volume.

Acronym	Meaning
AMSR-E / AMSR2	Advanced Microwave Scanning Radiometer (for EOS / #2)
AMSRs	Both AMSR-E and AMSR2
CCI	Climate Change Initiative
CDR	Climate Data Record
DAL	Distance Along the (sea-ice) Line
DMSP	Defence Meteorological Satellite Program
EASE grid	Equal-Area Scalable Earth Grid
ECMWF	European Centre for Medium-Range Weather Forecasts
ESA	European Space Agency
ESMR	Electrically Scanning Microwave Radiometer
EUMETSAT	European Organization for the Exploitation of Meteorological Satellites
FCDR	Fundamental Climate Data Record
FoV (<i>alt</i> FOV)	Field-of-View
FYI	First Year Ice
ICDR	Interim Climate Data Record
L1B, L2, L3, ...	Satellite data processing Level (Level-1b, ...)
EPS, EPS-SG	EUMETSAT's Polar System, EPS Second Generation
MWI	MicroWave Imager (EPS-SG)
MYI	Multi-Year Ice
NSIDC	US National Snow and Ice Data Centre
OSI SAF	EUMETSAT Ocean and Sea Ice Satellite Application Facility
OWF	Open Water Filter
PMR	Passive Microwave Radiometer
PMW	Passive Microwave
RTM	Radiative Transfer Model
SIC	Sea Ice Concentration
SMMR	Scanning Multichannel Microwave Radiometer
SSM/I	Special Sensor Microwave/Imager
SSMIS	Special Sensor Microwave Imager/Sounder
SSM/IS	Both SSM/I and SSMIS sensors

Table 1: Acronyms and Abbreviations. Acronyms for the deliverable items (URD, etc...) and partner institutions (AWI,..) are not repeated.

1.5 Executive Summary

The present ATBD documents the algorithms developed during the ESA CCI+ Sea Ice Phase 1 project (2019-2022) for the Sea Ice Concentration (SIC) variable. The focus of the CCI programme is the generation of long-term, time consistent Climate Data Records (CDRs), not the production of near-real-time data products. In the case of Sea Ice Concentration, this translates into a focus on three distinct themes:

- Preparing high(er) spatial resolution sea-ice concentration CDRs using the near-90 GHz imagery of the SSM/IS (1991-2000) and AMSRs (2002-2020) missions. This development is closely connected to the developments at the EUMETSAT OSI SAF towards their SIC CDR v3.
- Preparing a sea-ice concentration CDR from the Electrically Scanning Microwave Radiometer (ESMR) for the period 1972-1977. This is a key development to gain better insights in sea-ice evolution in the early 1970s.
- Preparing algorithms for a better monitoring of the sea-ice conditions during the Arctic summer melt period. These algorithms are developed during the CCI+ Sea Ice Phase 1 project, but are not applied in the CDRs.

The following chapters describe these sections in turn.

2 HIGH(ER) RESOLUTION SIC USING THE NEAR-90 GHz IMAGERY (1991 - 2020)

2.1 Complementarity and relation to EUMETSAT OSI SAF SIC data

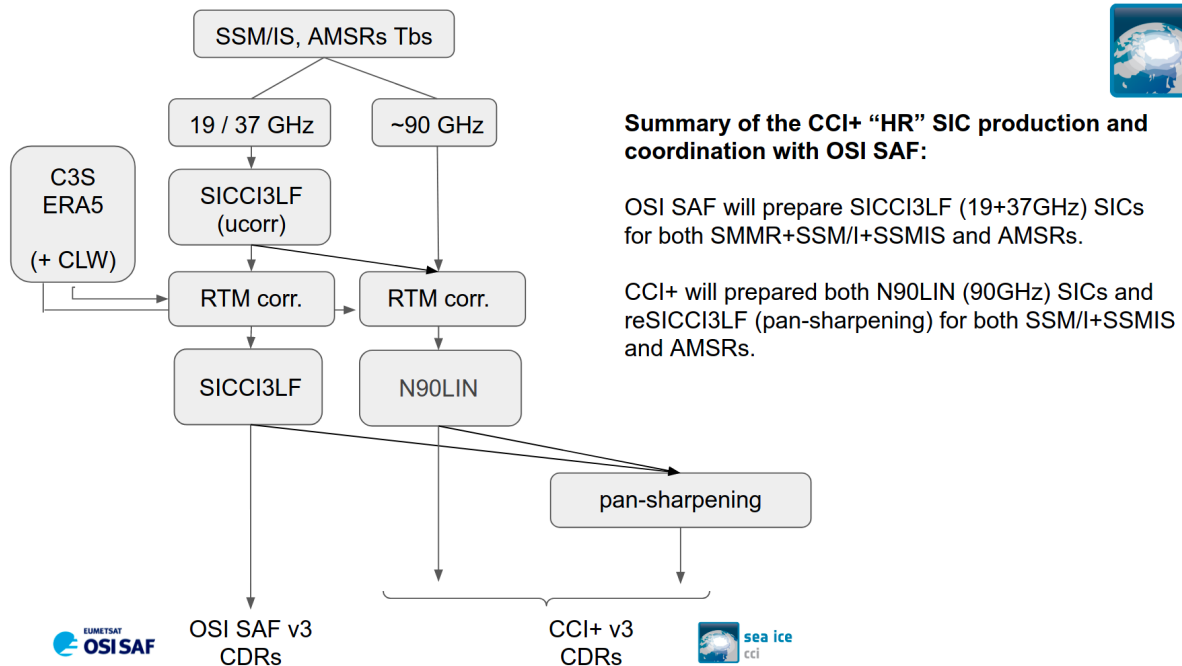


Figure 1: Schematic of the complementarity and relation between the EUMETSAT OSI SAF and ESA CCI+ Sea Ice Concentration datasets for v3 (2021/22).

Figure 1 is a schematic of the complementarity and relation between the EUMETSAT OSI SAF and ESA CCI+ Sea Ice Concentration processing and products for the v3 CDRs. At the top are the input satellite data from a series of passive microwave missions namely SMMR, SSM/I, SSMIS, AMSR-E and AMSR2. Except for SMMR (1978-1987) which is only used in the OSI SAF CDRs, all other missions are exploited by both projects.

For the “v3” CDRs, the complementarity between OSI SAF and CCI+ Phase 1 is in the type of algorithms being applied, and thus the target spatial resolution: OSI SAF applies the “19/37 GHz” algorithms (SICCI3LF on Figure 1) to both SSM/Is and AMSRs. These algorithms were the basis for the “v2” CDRs OSI-450 and SICCI-25km (Lavergne et al., 2019). Meanwhile, CCI+ Phase 1 focuses on the “near-90 GHz” imagery using both SSMIS and AMSRs. These imagery channels offer a higher spatial resolution but also result in larger retrieval errors, and are only available from the early 1990s. The CCI+ Phase 1 SIC production has two streams: N90LIN, and pan-sharpening. The N90LIN step prepares SICs relying mostly on the near-90 GHz channels (higher resolution, higher noise). The pansharpening step prepares SICs using the results of both SICCI3LF and N90LIN (higher resolution, less noise). The result of the pan-sharpening step (named “resolution enhanced” SICCI3LF, reSICCI3LF) is a main SIC outcome from CCI+ Phase 1, while N90LIN is more seen as a by-product for expert users (because of the increased noise).

In this ATBD, we shall focus on the algorithm parts that are specific to CCI+ datasets (N90LIN and pan-sharpening) and refer to the OSI SAF ATBD for the description of the SICCI3LF algorithms. When the N90LIN algorithm uses algorithm steps that are shared with the SICCI3LF algorithms (e.g. same algorithm step, but with different microwave frequency channels) we will also refer to the OSI SAF ATBD.

The OSI SAF SIC ATBD is:

[REF-1]: EUMETSAT OSI SAF: Algorithm Theoretical Basis Document for the OSI SAF Global Sea Ice Concentration Climate Data Records (OSI-450-a, OSI-430-a, OSI-458), SAF/OSI/CDOP3/DMI_Met/SCI/MA/270, v2.1, June 2021

2.2 Satellite and auxiliary data

Satellite data

SIC fields are processed from passive microwave radiometer missions of the types SSM/I (DMSP F10 to F15), SSMIS (DMSP F16 to F18), AMSR-E (NASA Aqua) and AMSR2 (JAXA GCOM-W1). The SMMR mission (1978-1987) did not have near-90 GHz imagery channels, and the first SSM/I (DMSP F08, Jul 1987 – Dec 1991) and mal-functioning near-90GHz imagery channels and are thus not used in the CCI+ Sea Ice Phase 1 SIC dataset.

Detailed information about the satellite missions can be found in the OSI SAF ATBD [REF-1], specifically sections 2.2 (SSM/I), 2.3 (SSMIS), 2.4 (AMSR-E) and 2.5 (AMSR2). Figure 2 shows a timeline of the passive microwave missions relevant for SIC monitoring, including those used in the CCI+ Sea Ice Phase 1 CDRs.

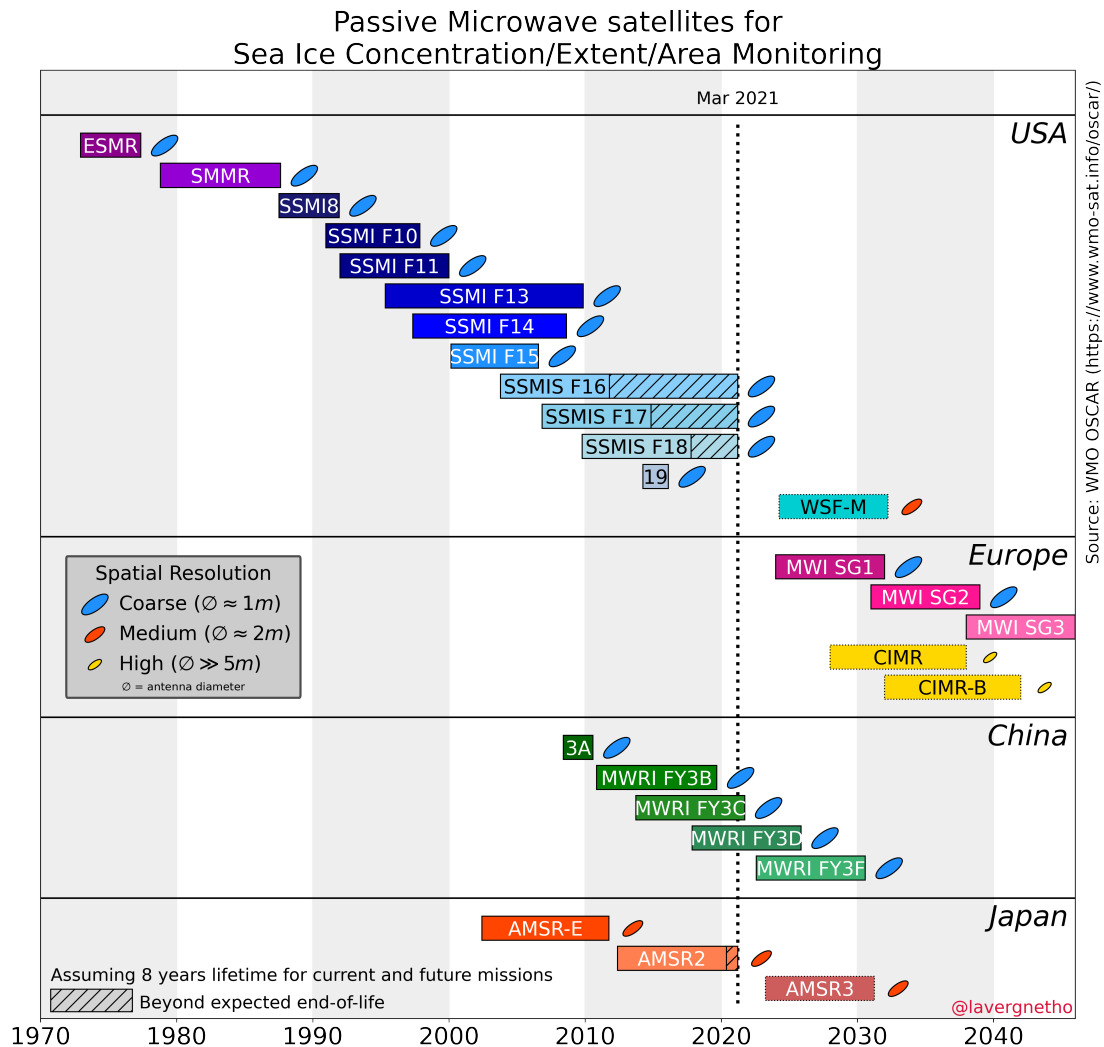


Figure 2: Timeline of the Passive Microwave satellite missions relevant for sea-ice concentration/extent/area monitoring with an indication of their spatial resolution capabilities. The CCI+ Sea Ice Phase 1 “v3” CDRs use the SSM/I (from F10), the SSMIS (F16-F18), the AMSR-E and AMSR2 missions. The horizontal bars represent satellite missions, that are colored by sensor family. Credit: T. Lavergne.

Thanks to their larger reflector antenna, the AMSR-E and AMSR2 missions bring higher spatial resolution than the SSM/IS missions at all frequencies. As in previous versions of the CDRs, we do not attempt to merge SIC products from AMSRs with those from SSM/IS.

Atmosphere reanalysis data

A key step in our processing chains is the explicit correction of brightness temperatures using a Radiative Transfer Model (RTM). This step reduces the retrieval noise in SIC, and requires auxiliary information from an atmosphere reanalysis.

For “v3” we use fields of surface temperature (T2m), wind speed (10m), total columnar water vapour (TCWV) and total columnar liquid water (TCLW) from the C3S/ECMWF ERA5

reanalysis (Hersbach et al., 2020).

Land masks

To ensure consistency between the OSI SAF and CCI+ Sea Ice “v3” data records, they use a common land mask.

The land mask is derived from the CCI Sea Surface Temperature OSTIA v2 0.05°x0.05° global mask for land/ocean boundary, and the CCI Lakes v1 0.0083°x0.0083° global mask for the land/lakes boundaries. These two fine resolution masks are first aggregated into a series of area density masks (area density of ocean, lakes, and land) at 12.5x12.5 km resolution. Then a binary “smask” (surface mask) field is prepared using a threshold of 0.3 (smask shows ‘land’ if the area density of land is larger than 0.3). The value of 0.3 was tuned against the binary land mask of the US NSIDC Sea Ice Concentration Climate Data Record (Peng et al., 2013; Meier et al., 2017). Only the US Great Lakes and Caspian Sea are kept as lakes, because most other lakes are too small wrt to the resolution of the passive microwave channels used in these CDRs.

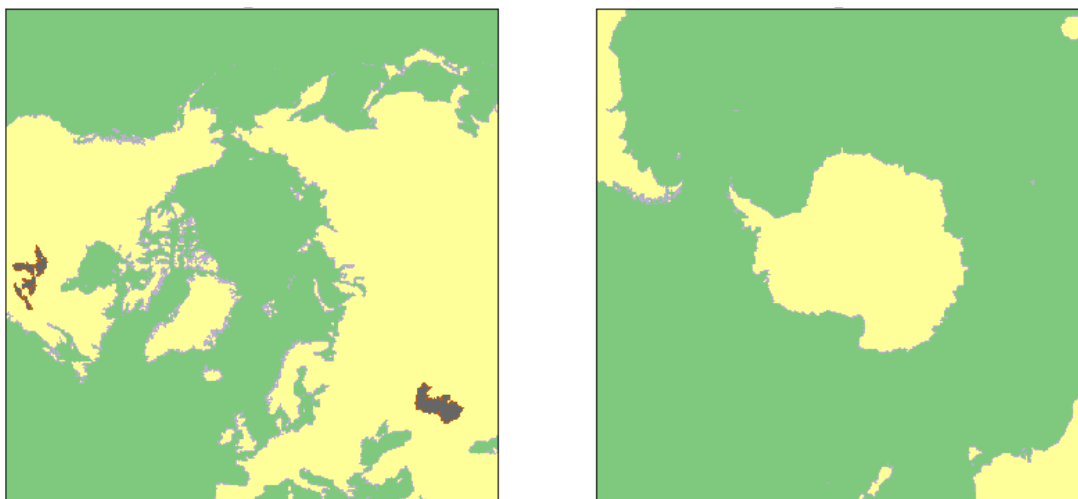


Figure 3: Variable "smask" used in the SIC CDRs on the EASE2 12.5 km grids (left: NH, right: SH). Ocean (smask=0): green, Ocean coastline (smask=1): light grey, Land (smask=2): yellow, Lake coastline (smask=4): red, Lake (smask=5): dark grey.

Maximum sea ice extent climatology

The monthly-varying maximum sea-ice extent climatology mask is common to the OSI SAF and CCI+ Sea Ice “v3” CDRs.

Spurious sea-ice concentration in open sea at low latitudes (caused by high water vapour content) and along the coasts at mid to high latitudes (caused by land spill-over contamination of the brightness temperatures) require using a maximum sea ice extent climatology mask. Ocean grid cells outside the mask are assigned a SIC of 0%.

The climatology we use is adapted from that of the NSIDC SIC CDR (Peng et al., 2013; Meier et al., 2017). They are then cleaned by visual inspection using sea-ice charts from the

US National Ice Center, Canadian Ice Service, and Norwegian and Finnish Ice Services (e.g. along the coast of northern Norway, for some summer months in the vicinity of Nova Scotia and in the Baltic Sea and Gulf of Finland). The cleaned climatologies are re-projected from their polar-stereographic projection to the EASE2 grids, and expanded with a buffer zone of 150 km in the NH and 250 km in the SH. This expansion is not applied in the Baltic Sea during the summer months.

2.3 The near-90 GHz linear (N90LIN) SIC algorithms

The processing algorithms for the N90LIN algorithms are very similar to those described in the OSI SAF ATBD, except that the OSI SAF ATBD describes them in the 3-dimensional brightness temperature space (19V, 37V, 37H) sustaining the SICCI3LF algorithm, while the N90LIN algorithm works in the 2-dimensional space (90V, 90H).

Others than that, the description in the OSI SAF ATBD are directly applicable for the N90LIN SIC algorithms. Figure 4 gives an overview of the full processing chain for the N90LIN SIC algorithms. We refer to the OSI SAF ATBD for the full description of the steps, and describe below the most noticeable differences.

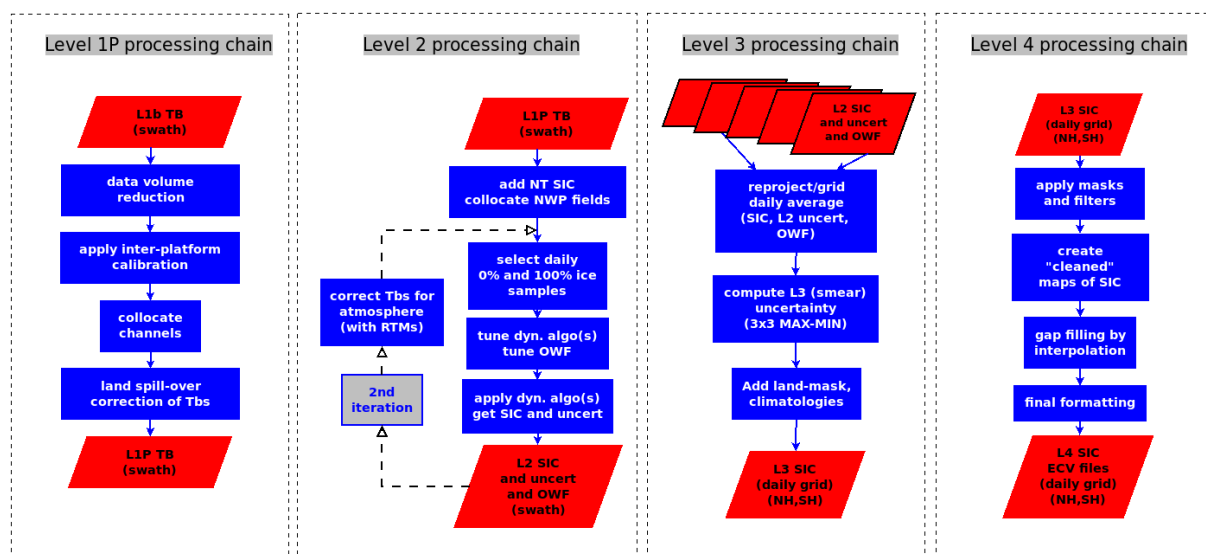


Figure 4: From left to right, the four main elements (Level 1P, Level 2, Level 3, and Level 4) in the sea-ice concentration (SIC) processing workflow. The red boxes depict data files, the blue boxes correspond to individual steps (a.k.a. algorithms) in the processing. The files that exit a processing chain (e.g. the “L2 SIC and uncert and OWF” at the bottom of the Level 2 processing chain) are the input for the next level of processing. Acronyms: NT is the Nasa Team algorithm, OWF is open-water filter, RTM is radiative transfer model, uncert stands for uncertainty.

Pre-processing on swath projection (L1P)

The L1P processing is exactly the same as described in the OSI SAF ATBD [REF-1, section 4] and as a matter of facts is applied only once as a common step for both the OSI

SAF and the CCI+ Sea Ice climate data records.

Geophysical processing in swath projection (L2)

The main geophysical processing is in the L2 chain, which is where most differences to the OSI SAF ATBD are.

As in the OSI SAF ATBD ([REF-1, section 5.1]) we use the formulation of a *hybrid* SIC algorithm to combine two optimized algorithms: one that is tuned to perform better over open-water and low-concentration conditions (named B_{OW} for “best open water”), and one that is tuned to perform better over closed-ice and high-concentration conditions (named B_{CI} for “best closed ice”).

$$SIC_{hybrid} = w_{OW} * B_{OW} + (1 - w_{OW}) * B_{CI} \quad (1)$$

$$\left\{ \begin{array}{l} w_{OW} = 1 \text{ for } B_{OW} < 0.7 \\ w_{OW} = 0 \text{ for } B_{OW} > 0.9 \\ w_{OW} = \frac{B_{OW} - 0.7}{0.2} \text{ for } B_{OW} \in [0.7; 0.9] \end{array} \right. \quad (2)$$

The formulation of each of B_{OW} and B_{CI} follows:

$$C(\vec{T}) = \frac{\vec{v} \cdot (\vec{T} - \langle \vec{T}^W \rangle)}{\vec{v} \cdot (\langle \vec{T}^I \rangle - \langle \vec{T}^W \rangle)} \quad (3)$$

Where $\vec{T} = (T_{90v}, T_{90h})$ is a pair of brightness temperatures at the near-90 GHz frequencies in the horizontal and vertical polarizations, and corresponds to the N90LIN algorithm. In the OSI SAF ATBD, Eq. 3 was introduced using $\vec{T} = (T_{19v}, T_{37v}, T_{37h})$, the triplet corresponding to the SICCI3LF algorithm.

The dynamic tuning of the N90LIN algorithms can be described similarly as in [REF-1, section 5.1.3 and 5.1.4]: training samples of known open-water (0% SIC) and assumed consolidated ice (100% SIC) conditions over a [-7;+7 days] sliding period are selected and enter the tuning procedure. They are used to derive the two tie-points $\langle \vec{T}^W \rangle$ (open water tie-point) and $\langle \vec{T}^I \rangle$ (consolidated ice tie-point) as well as \vec{u} (unit vector sustaining the ice line). In contrast to the tuning of the SICCI3LF, however, vector \vec{v} in Eq. 3 cannot be optimized in the two-dimensional space of N90LIN: using 2 channels we can only select \vec{v} as perpendicular to \vec{u} . In the three-dimensional space of the SICCI3LF tuning, there are an infinite number of unit vectors \vec{v} that are perpendicular to \vec{u} and an optimization can be performed (see Figure 3 in Lavergne et al., 2019).

At the end of the tuning (which is repeated on a daily basis), the tie-points $\langle \vec{T}^W \rangle$ and $\langle \vec{T}^I \rangle$ are stored, as well as vectors \vec{v}_{OW} and \vec{v}_{CI} . This is all what is needed to later apply the B_{OW} and B_{CI} algorithms on satellite swath data, and combine the results into the

hybrid SIC value (Eq. 1).

As described in Andersen et al. (2006) and confirmed in Ivanova et al. (2015), the accuracy of retrieved sea-ice concentration can be greatly improved when the brightness temperatures are corrected for atmospheric contribution by using a radiative transfer model (RTM) combined with surface and atmosphere fields from NWP reanalyses. Both the algorithms using the 19 and 37 GHz channels (like SICCI3LF) and those using the near-90 GHz channels (like N90LIN) have the potential to be improved by this technique (see Figure 6 in Ivanova et al., 2015).

For the CCI+ Sea Ice Phase 1 N90LIN product we perform the RTM-based correction as described in the [REF-1, section 5.2], thus with a double-difference scheme involving the Wentz (1997) and Wentz and Meissner (2000) RTMs. We use fields of surface temperature (T_{2m}), wind speed (10m), total columnar water vapour (TCWV) and total columnar liquid water (TCLW) from the C3S/ECMWF ERA5 reanalysis (Hersbach et al., 2020) as input to the RTM. Note that for the correction of N90LIN, we use the SIC resulting from the SICCI3LF algorithm as first-guess SIC (SIC_{ucorr}) (see the arrow from “SICCI3LF (ucorr)” to the “RTM correction” box in Figure 1). The corrected brightness temperature (T_{b,corr}) obtained at the end of this step are used as input to the N90LIN algorithm. This strategy of using a “low-frequency” SIC algorithm as a first-guess SIC for the double-difference correction is very similar to the strategy presented in Lu et al. (2018).

Figure 5 and Figure 6 illustrate the very large positive impact of the RTM-based atmospheric correction in both hemispheres over the Open Water conditions for the N90LIN algorithm. The correction with ERA5 data allows a reduction of the retrieval uncertainty from 30-40 % (1 standard deviation) to about 13 % for the Northern Hemisphere (15 % for the Southern Hemisphere). Comparing the uncorrected and corrected uncertainties in these two figures also reveals that the correction step seems to reconcile the various missions to a common level. Especially in the Southern Hemisphere (Figure 6) the uncertainty of the uncorrected N90LIN SICs is higher for SSMIS (light blue) and AMSRs (orange) than SSM/I (dark blue). This is probably related to the different microwave frequencies of these missions (section 2.2) with the SSM/I mission having slightly smaller frequency (85.5 GHz) than the two other (89 and 91 GHz).

The remaining N90LIN SIC uncertainty over Open Water condition after the atmospheric correction is still much higher than what is obtained from the SICCI3LF algorithms (2-3 % uncertainty after the atmospheric correction step), but the N90LIN brings the higher resolution of the near-90 GHz imagery channels. In the CCI+ Sea Ice Phase 1 project, the N90LIN SICs (after atmospheric correction) are distributed for the expert users to explore (because of the remaining high uncertainty), but also N90LIN enters the pan-sharpening step to bring an enhanced resolution field of SICs (Figure 1).

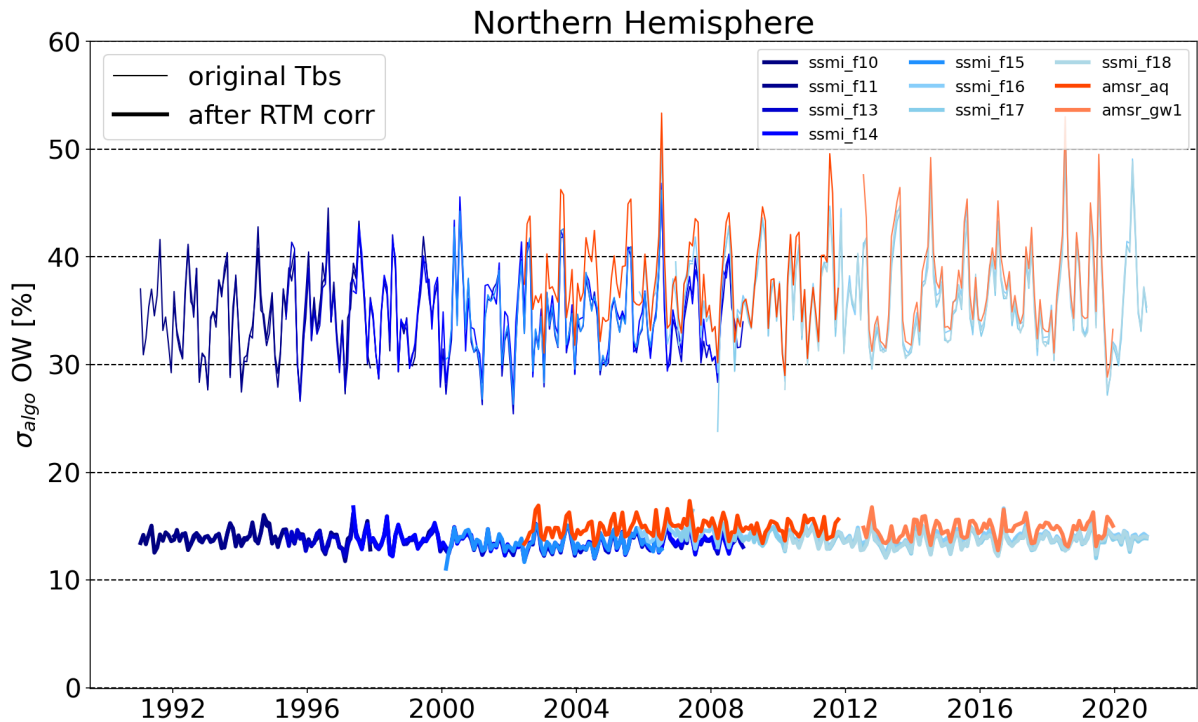


Figure 5: Timeseries of the SIC retrieval uncertainty σ_{algo} for OW conditions in the Northern Hemisphere over the period 1991-2020. Thin lines are for the SIC retrieval noise without atmospheric correction, and thick lines are with the atmospheric correction. Colors indicate the satellite missions (not all available missions were active during the period, see Figure 2).

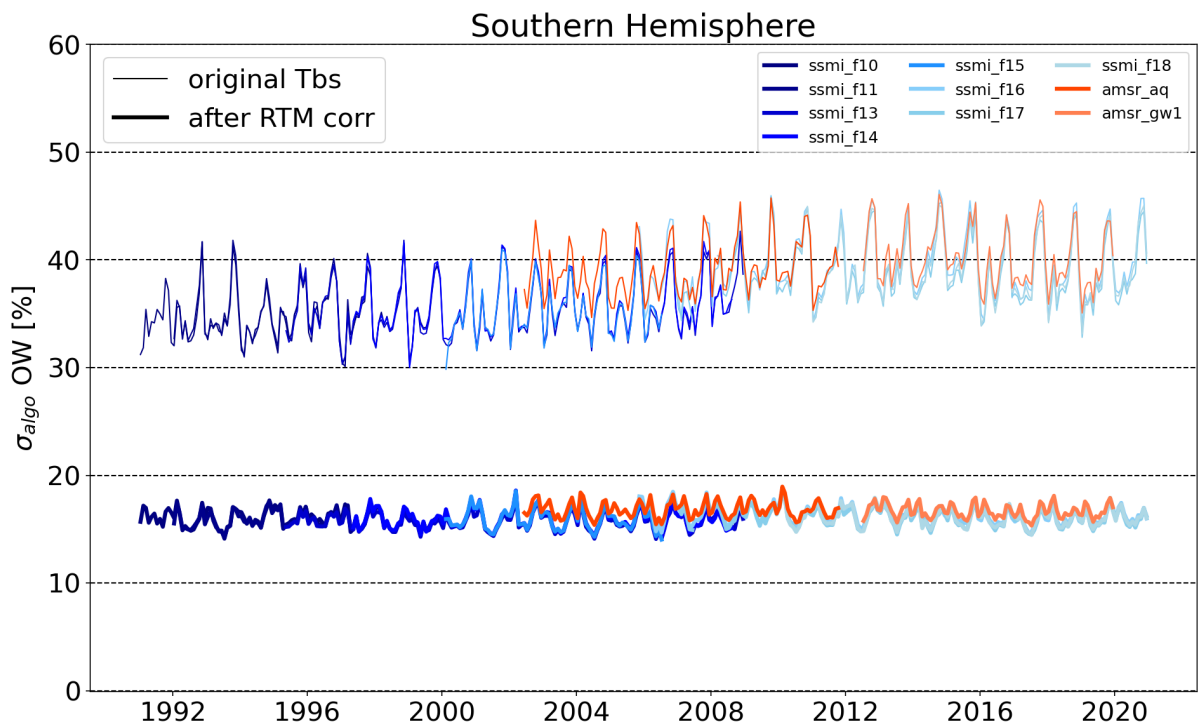


Figure 6: Same as Figure 5 but for the Southern Hemisphere.

The rest of the Level-2 algorithm steps (uncertainties, correction at high concentration range) is very similar to that already described in the OSI SAF SIC ATBD.

Level-3 and Level-4 algorithms

The Level-3 and Level-4 algorithms for our SIC processing chains does not depend on the microwave frequencies and are the same as described in the OSI SAF ATBD. The only noteworthy difference is that the SICCI3LF algorithms in the OSI SAF data records are prepared onto 25x25 km EASE2 grids, while the N90LIN fields in the CCI+ Sea Ice are prepared onto 12.5x12.5 km EASE2 grids.

2.4 Resolution-enhanced reSICCI3LF SIC fields using pan-sharpening

The previous sections and the OSI SAF ATBD described how two sea-ice concentration fields are prepared independently from the SSM/IS and AMSRs missions: SICCI3LF (using the ~19 GHz and ~37 GHz channels) and N90LIN (using the near-90 GHz channels).

In the CCI+ Sea Ice processing chains, we merge the two SIC fields (SICCI3LF and N90LIN) using a pan-sharpening technique (Meng et al. 2019). Pan-sharpening was introduced for improving the spatial resolution of high-resolution optical imagery missions such as SPOT in the 1980s. These types of mission typically offered a pan-chromatic imagery band with high spatial resolution (but covering a broad range of wavelengths) and multi-spectral imagery (narrower bandwidth but lower spatial resolution because less photons are recorded). Pan-sharpening techniques emerged for combining the fine details of the pan-chromatic imagery with the information content of the multi-spectral imagery to provide high-resolution multi-spectral imagery. Nowadays many pan-sharpening techniques exist for many missions (see e.g. a review in Meng et al. 2019).

In the field of sea-ice concentration monitoring from passive microwave radiometer data, pan-sharpening have been used recently in Ludwig et al. (2019) and Kilic et al. (2020). There are indications that a pan-sharpening technique was also used in one of the versions of the NORSEX algorithm (Svendsen et al. 1987).

We implement a simple pan-sharpening algorithm from the SICCI3LF and N90LIN fields at Level-3 (after gridding on the 12.5 km grid and daily averaging):

$$SIC_{reSICCI3LF} = SIC_{SICCI3LF} + (SIC_{N90LIN} - SIC_{N90LIN,blurred}) \quad (4)$$

In Eq. 4 all the SIC fields are on a 12.5 km grid spacing and the operations between the fields are thus at a grid-cell level. $SIC_{SICCI3LF}$ and SIC_{N90LIN} are directly the results of the two algorithms, while $SIC_{N90LIN,blurred}$ is a blurred version of the original N90LIN field.

$SIC_{reSICCI3LF}$ is the pan-sharpened SIC field (*aka* resolution-enhanced, *re*) which has the low retrieval noise of the SICCI3LF algorithm and the high(er) spatial resolution of the N90LIN algorithm.

The right-hand side of Eq. 4 has two terms: $SIC_{SICCI3LF}$ and a “delta” term which implements the pan-sharpening *per se*. The delta is between the original N90LIN SIC and a blurred version of that same field. Because the blurred N90LIN will differ from the original N90LIN only where there are gradients in the SIC field, the delta will be exactly 0 away from the gradients where $SIC_{reSICCI3LF}$ will exactly be $SIC_{SICCI3LF}$. The delta implements the pan-sharpening by adding or subtracting some amount of SIC on either side of the gradients, as illustrated in the bottom-left panel of Figure 7.

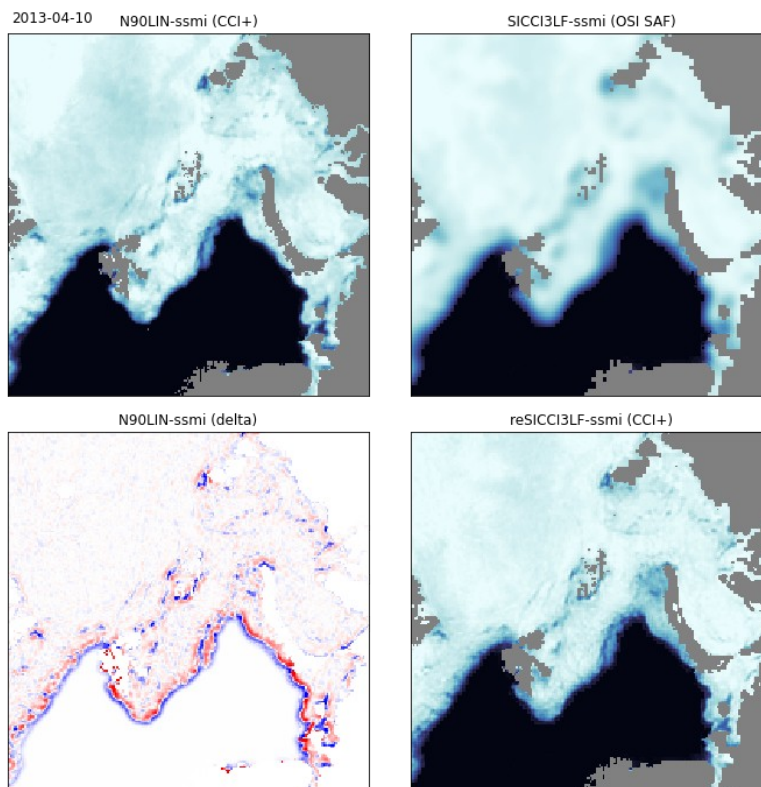


Figure 7: Illustration of the pan-sharpening process with SSM/I data in the Arctic on 10th April 2013. Top-left: N90LIN SIC (CCI+ v3), top-right: the SICCI3LF SIC (OSI SAF v3), bottom-left: the delta from Eq. 4, and bottom-right: the resulting reSICCI3LF SIC (CCI+ v3).

In Figure 7, the pan-sharpening process is illustrated and the increased resolution is shown (compare top-right: original SICCI3LF and bottom-right: reSICCI3LF).

For the “delta” to implement the correct amount of correction along the gradients, it is key that the *true* spatial resolution of $SIC_{N90LIN,blurred}$ is close to that of $SIC_{SICCI3LF}$. All the SIC fields in Eq. 4 are on a 12.5 km grid spacing, but their *true* spatial resolution is different.

The blurring is implemented with a gaussian filter and thus a specific σ , the standard deviation of the gaussian bell curve used as the filter. In the CCI+ Sea Ice project we designed an objective method to select an optimal blurring parameter σ . The optimization of σ involves transects of SIC across sharp edges in the MIZ both in the Arctic and Antarctic,

and in different seasons to capture a large range of conditions. SIC for the SICCI3LF and N90LIN fields are extracted along these transects and a series of σ are used to blur the N90LIN transect with a gaussian filter. The RMSD and correlation coefficient between each blurred transect and the original SICCI3LF is computed and tabulated. Positions along the transect where the SICs are less than 5% or greater than 95% are discarded to focus the comparison around the gradient. The σ allowing the best match (lower RMSD, highest correlation) between the transects is selected as the σ bringing the blurred SICCI3LF closest to SICCI3LF in terms of spatial features along the gradients of the MIZ.

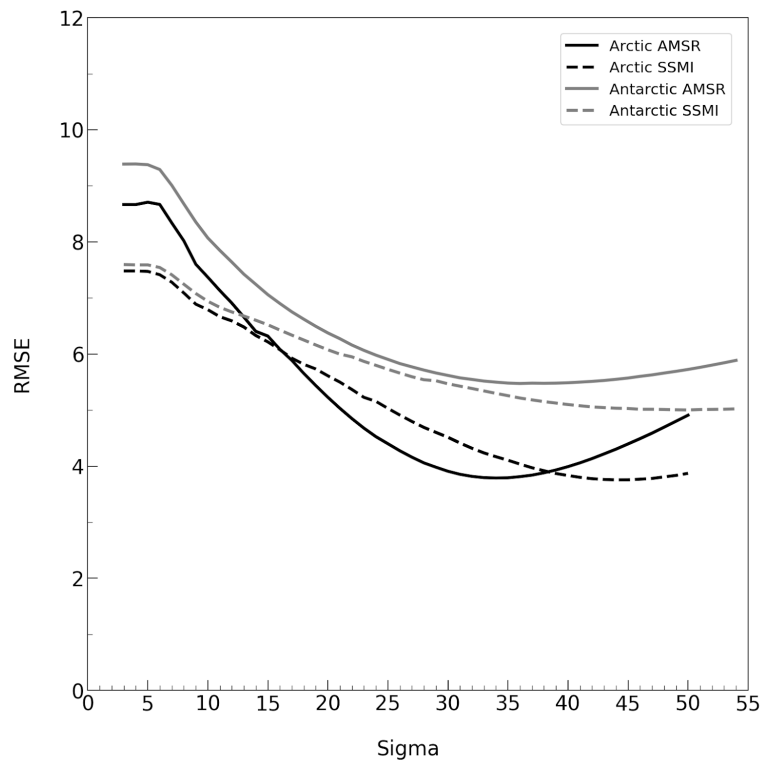


Figure 8: Objective optimization of the σ parameter of the gaussian filter used for blurring N90LIN in the pan-sharpening step. X-axis: sigma in km.

Figure 8 summarizes the results for the optimization of σ [km] for both SSMIS and AMSRs missions in the Arctic and Antarctic MIZ. The σ for the AMSR missions (at the minimum point of the solid lines) is smaller than that for SSM/IS (dashed lines) which is expected, AMSRs having higher spatial resolution than SSM/IS. On Figure 8, a difference is observed between the location of the minimum of the Arctic (black) and Antarctic (grey) curves but this difference is small with respect to the curvature of the curve around the minimum: a relatively broad range of σ values yield similar RMSEs. With this method we thus select two σ , one for AMSRs and one for SSM/IS (Table 2).

	SSM/IS	AMSRs
σ [km]	48	34

Table 2: Sigma of the gaussian averaging kernel used in the pan-sharpening step for SSM/IS instruments (SSM/I and SSMIS) and AMSRs (AMSR-E and AMSR2). The same value is used in the Northern and Southern Hemispheres.

2.5 Summary for the high(er) spatial resolution SICs using the near-90 GHz imagery channels.

This chapter of the ATBD described the algorithm steps required to prepare the SIC CDRs of the CCI+ Sea Ice Phase 1 project. The description refers heavily to the OSI SAF SIC ATBD [REF-1] for the many common algorithm steps.

For CCI+ Sea Ice Phase 1, we target high(er) spatial resolution SIC CDRs extending over the last 3 decades (1991-2020). This R&D effort is a direct response to the WMO GCOS requirements for the Sea Ice Concentration products, and a continuation of the work started with the SICCI-12km algorithms from CCI Sea Ice Phase 2.

We adopt a two-step strategy towards high(er) spatial resolution SIC CDRs in CCI+ Phase 1:

- 1) prepare a state-of-the-art high-resolution, high-noise SIC CDR using the near-90GHz imagery channels of SSM/IS and AMSRs (the N90LIN algorithm);
- 2) use this new N90LIN SIC CDR in combination with the the OSI SAF SIC CDR (based on the 19 and 37 GHz channels of SSM/IS and AMSRs) and produced a resolution-enhanced (12.5 km) SIC CDR with lower uncertainty than N90LIN (reSICCI3LF).

Figure 9 displays example fields obtained from the SSMIS F18 mission on 11 April 2019, showing from top to bottom the SIC obtained from the SICCI3LF algorithm (basis for the OSI SAF v3 CDR), the N90LIN algorithm (step 1 for CCI+ Sea Ice Phase 1) and the reSICCI3LF algorithm (combining SICCI3LF and N90LIN, step 2 for CCI+ Sea Ice Phase 2). Despite being from a prototype version of the processing chains, these examples highlight the improved spatial resolution to be delivered by the CCI+ Sea Ice Phase 1 CDRs.

Because we rely on the near-90 GHz imagery channels, the CCI+ Sea Ice Phase 1 SIC CDRs only cover the period 1991-2020 and are thus shorter than those of OSI SAF (1978-2020).

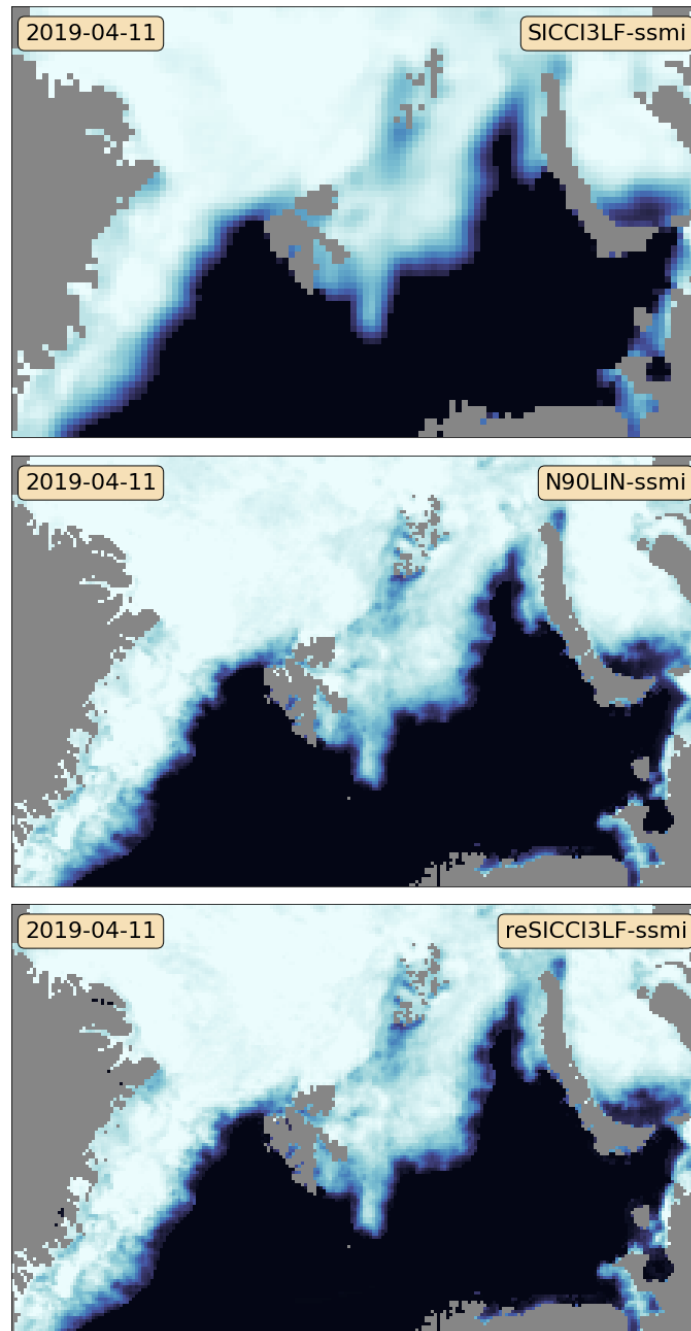


Figure 9: Examples of SIC fields valid for 11 April 2019 as derived from: (top) SICCI3LF algorithm (OSI SAF), (middle) N90LIN (CCI+) and (bottom) reSICCI3LF. The fields are from the SSMIS F18 mission. Note: these are from a prototype version of the processing chains, the fields in the final SIC CDRs might differ.

3 SEA ICE COVER WITH ESMR (1972 – 1977)

The Electrically Scanning Microwave Radiometer (ESMR) on board the NIMBUS 5 satellite was a one channel radiometer measuring 19.35 GHz horizontally polarized microwave thermal emission. It operated from 11. Dec. 1972 to 16. May 1977 (1617 days) with some interruptions. After a major data gap from 3. Jun. 1975 until 25. Aug. 1975 the instrument was only operated approximately every other day. The data have recently been made available online by NASA in the format which was used for the tape archive (TAP-files).

The experimental NIMBUS program was extremely successful and there is heritage from it in modern satellite programs. Even though ESMR was a predecessor of modern multi frequency radiometers there are still parts of modern processing methodologies which can be applied to the data to derive the sea ice extent globally. In fact, both the dynamical tie-points and the atmospheric noise reduction of the T_B 's can reduce the noise over ice and open water consistently and that is the reason for reprocessing the data. The ESMR data set can extend the sea ice climate data record with an important period in the 1970s.

The ESMR instrument was a cross-track scanner measuring at 78 scan positions from nadir to an incidence angle of about 63 degrees perpendicular to both sides of the flight track (39 scan positions to the right and left of the flight track). The near circular orbit height was about 1112 km with an inclination of 81 degrees. The phased array antenna size was 85.5 x 83.3 cm and the spatial resolution about 25 km at nadir increasing to about 160 x 45 km at the edges of the swath. The full swath was about 3100 km with varying incidence angle and spatial resolution giving a very good (unprecedented) daily coverage in polar regions.

3.1 Input and auxiliary data

The ESMR data were retrieved from the NASA Goddard Earth Sciences Data and information services center (GES DISC) online data archive (https://disc.gsfc.nasa.gov/datasets/ESMRN5L1_001/summary).

The TAP files were read using NASA software and converted to NetCDF format. Each data point in the TAP file was matched up with ERA40 data in time and space (nearest) and written to the NetCDF file. The data are structured line by line (across-track) the list below is summarizing the variable names and their meaning.

Satellite variables

Time	time of data
Brightness_temperature	Brightness temperature of the 78 scan spots
Latitude	latitude of the 78 scan spots [degrees]
Longitude	longitude of the 78 scan spots [degrees]
Pitch_fine_error	Pitch fine error

Roll_fine_error	Roll fine error
RMP_rate	RMP indicated rate high
NADIR_LAT	Sub-satellite latitude
NADIR_LON	Sub-satellite longitude
Height	Satellite height [km]
Digital_b	is a set of 1 bit status words to indicate the position of each of the command relays (users guide p. 83)
Status_indicator_1	-
Status_indicator_2	-
Data_source	-
Beam_position	-
PGM_id	Unique identification number assigned to program that prepared tapes
HOT_MEAN	hot load mean
HOT_RMS	rms of hot load
COLD_MEAN	cold load mean
COLD_RMS	rms of cold load
MUX_1	Average antenna temperature
MUX_2	Average phase shifter temperature
MUX_3	Ferrite switch temperature
MUX_4	Ambient load temperature
MUX_5	Reference load temperature
MUX_6	Automatic Gain Control
Analog_0	analog signals (voltages) of engineering interest
Analog_1	analog signals (voltages) of engineering interest
Analog_2	analog signals (voltages) of engineering interest
Analog_3	analog signals (voltages) of engineering interest
Analog_4	analog signals (voltages) of engineering interest
Analog_5	analog signals (voltages) of engineering interest
Analog_6	analog signals (voltages) of engineering interest
Analog_7	analog signals (voltages) of engineering interest

Analog_8	analog signals (voltages) of engineering interest
Analog_9	analog signals (voltages) of engineering interest
Analog_10	analog signals (voltages) of engineering interest
Analog_11	analog signals (voltages) of engineering interest
Analog_12	analog signals (voltages) of engineering interest
Analog_13	analog signals (voltages) of engineering interest
Analog_14	analog signals (voltages) of engineering interest
Analog_15	analog signals (voltages) of engineering interest

ERA40 variables

u10	U component of the wind speed at 10 m (parallel to longitude)
v10	V component of the wind speed at 10 m (parallel to longitude)
t2m	2 m air temperature
istl1	ice internal temperature
istl2	ice internal temperature
istl3	ice internal temperature
istl4	ice internal temperature
lsm	land-sea-mask
msl	mean sea level pressure [hPa]
siconc	sea ice concentration [0,1]
sst	sea surface temperature [K].
skt	skin temperature [K]
tcw	total column water [kgm ⁻²]
tcwv	total column water vapor [kgm ⁻²]
era_time	valid time for analysis

3.2 Overview of the processing chain

The processing of ESMR TAP data for deriving the sea ice concentration is following the sequential processing steps:

1. the data in TAP format is converted NetCDF format retaining all variables and the data structure
2. each data-point is collocated with ERA40 re-analysis data in time and space retaining

the data structure

3. data filtering and correction
4. tie-points both corrected and uncorrected are computed
5. sea ice concentration and algorithm uncertainty is computed
6. re-sampling of swath data
7. uncertainties, land-spill-over, and flags are computed
8. the grids are written in NetCDF format

3.3 Pre-processing of the data

ESMR provided data from the same afternoon as it was launched on 11. Dec. 1972 until 16. May 1977 (1617 days) with some interruptions. A set of filters and one correction is applied before the data enters the sea ice processing chain. The unfiltered data set contains 13483 data files and after filtering there are 7362 (54%) good files left.

The filters that we apply are described in Sievers et al. (2020). They are applied in the same order as described and if only a single pixel or a couple of rows are flagged by the filtering only these pixels or rows are removed from the file. If the whole file is corrupted then it is deleted.

The analog filter is filtering 16 analog voltage entries in the data (Analog_0 - Analog_15) (Sabatini, 1972). Spikes in these analog signals correspond to anomalous brightness temperatures and the “analog” filter is computing the absolute gradient in the analog signals and anything over the value 10 is removed.

A set of filters are using the processed brightness temperatures in Kelvin. Good data are defined as:

$$90 < T_B < 274 \quad (5)$$

and

$$50 < \text{mean}(|\text{row}_{i+1} - \text{row}_i|) \quad (6)$$

where row is a across track row of T_B and i is an index along track

$$150 < |p_i - p_{i-1}| + |p_{i+1} - p_i| \quad (7)$$

where p is a single data-point T_B and i is an along track index.

$$|p_{i+6} - p_{i+5}| + |p_{i+5} - p_{i+4}| + |p_{i+4} - p_{i+3}| + |p_{i+3} - p_{i+2}| + |p_{i+2} - p_{i+1}| + |p_{i+1} - p_i| \neq 0 \quad (8)$$

After filtering a latitudinal dependent vertical striping in the data was corrected. The odd and even data-points across track gradient difference has a latitude dependent bias. A correction model was applied which largely removes the striping (Sievers et al., 2020).

Additionally the 4 outer data-points of the swath in both sides are removed. These correspond to incidence angles between 64 and 57 degrees and the outer edges of the swath is then starting at 56 degrees after removal. The outer data-points which are removed have coarse resolution and increased noise levels compared to near nadir data-points (Veng, 2021).

3.4 Level-2 algorithms

The level 2 algorithms include the radiative transfer model, the tie-points and geophysical noise reduction, and the sea ice concentration algorithms.

The radiative transfer model

The radiative transfer model (RTM) is taking as input: atmospheric columnar water vapor V [kgm^{-2}], 10 m wind speed W [m/s], atmospheric columnar cloud liquid water L [kgm^{-2}], sea surface temperature T_s [K], ice emitting layer temperature T_i [K], sea ice concentration c_{ice} [0-1], and incidence angle θ [deg]. In return it simulates the 19.4 GHz T_B at horizontal polarization. The model is comparable to the RTM's used for regional sea ice concentration noise reduction in Andersen et al. (2006), Tonboe et al. (2016), and Lavergne et al. (2019).

$$T_{B, simulated} = RTM(V, W, L, T_s, T_i, c_{ice}, \theta) \quad (9)$$

The RTM is using the atmospheric part of Wentz (1997) for computing atmospheric emission, transmissivity and reflectivity at the sea surface.

The sea ice surface emissivity is produced from a simulation using a combined sea ice thermodynamic and emission models during Arctic winter on first-year ice. The set-up and the simulations are described in Tonboe (2010). The emissivities as a function of incidence angle are shown in Figure 10.

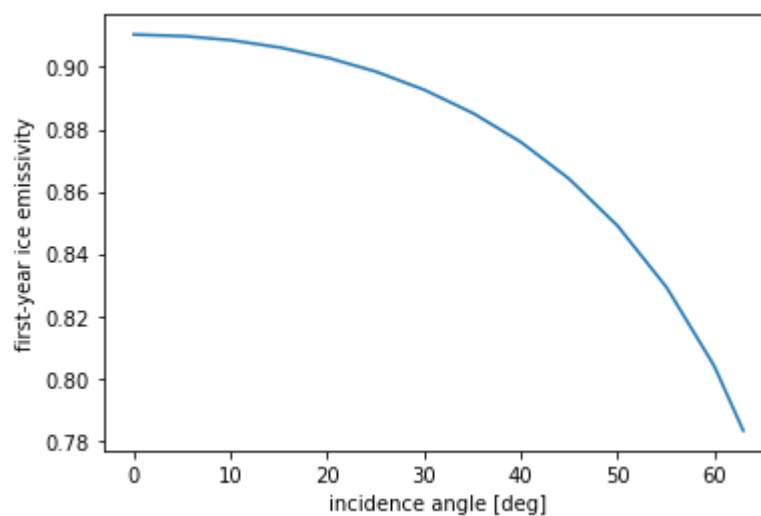


Figure 10: The first-year sea ice emissivity as a function of incidence angle.

The sea water permittivity as a function of temperature is tabulated from Eq. E64 (p. 2046) in Ulaby et al. (1986) and shown in Figure 11. The water salinity does not affect the permittivity at 19 GHz but 34 ppt is anyway used in the simulation.

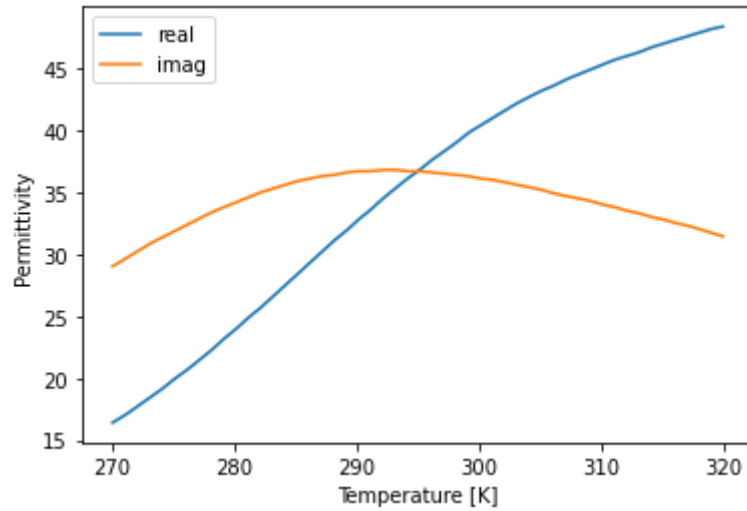


Figure 11: The sea water permittivity (real and imaginary parts) using equation E64 (p. 2046) in Ulaby et al. (1986).

The calm sea (Fresnel) reflection coefficient, r_h , as a function of the incidence angle θ for a lossy medium, is computed using Eq. 1.52 in Schanda (1986). The calm sea emissivity, E_0 , is then

$$E_0 = 1 - |r_h| \quad (10)$$

The rough water surface emissivity component, E_w , which is added to the calm sea emissivity, E_0 , to produce the total sea water emissivity, E_{water} , is from Meisner and Wentz (2012) with an additional angular term, i.e.

$$E_w = \frac{W(0.0094\theta + 0.3)}{Ts} \quad (11)$$

and

$$E_{water} = E_0 + E_w \quad (12)$$

where θ is the incidence angle in degrees, W is the wind speed [m/s], and Ts is the sea surface temperature [K].

The brightness temperature is a linear combination of the sea water and sea ice emission weighted by the sea ice concentration following Andersen et al. (2006)

$$T_{B, simulated} = T_{BU} + \tau(1 - c_{ice})E_{water}Ts + (1 - c_{ice})(1 - E_{water})(\Omega T_{BD} + \tau T_{BC}) + c_{ice}E_{ice}Ti + c_{ice}(1 - E_{ice})(T_{BD} + \tau T_{BC}) \quad (13)$$

where T_{BU} is the up-welling brightness temperature from the atmosphere, τ is the

transmissivity of the atmosphere, E_{water} is the water surface emissivity, E_{ice} is the sea ice emissivity, Ω is the reflection reduction factor due to water surface roughness, T_{BD} is the down-welling brightness temperature, T_{BC} is the cosmic background brightness temperature (2.7 K).

Tie-points and geophysical noise reduction

Tie-points are typical signatures of 100% ice and open water (0% ice) which are used in the sea ice concentration algorithm as a reference for estimating c_{ice} . The ESMR tie-points have been derived on a daily basis from the swath files and subsequently combined into 15-day running mean tie-points, 7 days ahead and 7 days behind the processed date. The 15-day averaging period has been maintained even when there are data gaps.

Four different regions have been selected for deriving tie-points: Arctic and Antarctic sea ice and Arctic and Antarctic open water. Land and ice shelves have been excluded. The selection of points in the swath file for the four tie-points is based on sea ice concentration, distance from ice edge and surrounding points, brightness temperature, latitude and sea surface temperature:

Arctic:

$$90^\circ > \text{latitude} > 32^\circ$$

Antarctic:

$$-90^\circ < \text{latitude} < -48^\circ$$

Ice:

sea ice concentration (ERA40) > 0.8 AND

the mean sea ice concentration (ERA40) of a 5 x 5 grid point box > 0.8 AND

100 K < brightness temperature < 274 K

Ocean:

sea ice concentration (ERA40) = 0 AND

the mean sea ice concentration (ERA40) of a 5 x 5 grid point box < 0.01 AND

the sea surface temperature (ERA40) < 278 K AND

50 K < brightness temperature < 180 K

The assumption about the tie-points is that they represent typical signatures of 100% ice and open water and we can therefore correct the tie-point T_B 's for geophysical noise using the RTM and the ERA40 reanalysis data. The per grid-point T_B correction term $\Delta T_{B, simulated}$ is the difference between a simulated reference T_B using mean values as input to the RTM and a simulated T_B using the actual ERA40 values for the grid-point. The correction term is added to the measured T_B in a one step procedure, i.e.

$$T_{B,corrected} = T_{B,measured} + \Delta T_{B,simulated} \quad (14)$$

where

$$\Delta T_{B,simulated} = RTM(\bar{V}, \bar{W}, \bar{L}, \bar{T}_s, \bar{T}_i, c_{ice}, \theta) - RTM(V, W, L, T_s, T_i, c_{ice}, \theta) \quad (15)$$

where V is the total column water vapor in the atmosphere [$kg\ m^{-2}$], W is 10 m wind speed [m/s], L is total column water vapor in the atmosphere [$kg\ m^{-2}$], T_s is the sea surface temperature [K], T_i is the ice emitting layer temperature [K] (Mäkynen, 2019), i.e.

$$T_i = 0.4 * T_{2m} + 0.6 * 272 \quad (12),$$

where T_{2m} is the 2 m air temperature [K], c_{ice} is 0 for the open water tie-point and 1 for the ice tie-point. The horizontal bars above the variable indicate that they are average values. The difference between the two model simulations minimizes the impact of biases in the model.

The (ERA40) L does not reduce noise in the data and therefore we do not correct for L . The L mean is used both in the reference and the actual simulation yielding zero impact while placing the simulated point correctly in model space. On average (for each day and each tie-point area) the $\Delta T_{B,simulated}$ is near 0.

The sea ice concentration

The sea ice concentration (c_{ice}) is estimated using the measured brightness temperature ($T_{B,measured}$) and the open water ($T_{p,water}$) and ice ($T_{p,ice}$) tie points, i.e.

$$c_{ice} = \frac{T_{B,measured} - T_{p,water}}{T_{p,ice} - T_{p,water}} \quad (16)$$

However because of the geophysical noise reduction using the radiative transfer calculation, needs c_{ice} as input, the sea ice concentration is processed iteratively in two steps: 1) the c_{ice} is estimated using uncorrected T_B 's and tie-points derived from uncorrected data. The c_{ice} estimate is truncated to the interval between 0 and 1 and an open water filter is applied forcing all c_{ice} values less than 0.15 to 0. 2) The c_{ice} estimate from step (1) is used in the radiative transfer calculation together with ERA40 data for for the geophysical noise reduction of the brightness temperatures and c_{ice} is then estimated again in a second iteration this time using corrected brightness temperatures and corrected tie-points. The mean values of $\bar{V}, \bar{W}, \bar{L} \dots$ used in the reference simulation is a weighted average with c_{ice} of the mean water and ice tie-point values for the respective variables.

3.5 Level-3 algorithms

The level-3 processing include the uncertainty algorithm.

The sea ice concentration uncertainty

The total sea ice concentration uncertainty is the combination of two components: 1) the

algorithm uncertainty which includes instrument noise and tie-point variability (geophysical noise) and 2) the re-sampling uncertainty which is uncertainty due to data re-sampling.

The algorithm uncertainty is the squared sum of three components following Parkinson et al. (1987) except the instrument noise term which is included in the other two terms in our implementation:

$$\delta c_{ice,algorithm} = \left(\left(\frac{-(1-c_{ice})\delta T_{p,water}}{T_{p,ice}-T_{p,water}} \right)^2 + \left(\frac{-c_{ice}\delta T_{p,ice}}{T_{p,ice}-T_{p,water}} \right)^2 \right)^{1/2} \quad (17)$$

where $\delta T_{p,water}$, is the water tie-point error, here the (one) standard deviation of the daily tie-point, $\delta T_{p,ice}$, is the ice tie-point error here the (one) standard deviation of the daily tie-point. The water and ice tie-point errors are weighted with the sea ice concentration and all three errors are normalized with the ice - water brightness temperature contrast here the 2-weekly ice – water tie-point difference. The algorithm uncertainty is computed on swath data and re-sampled using nearest to the grid-point sampling (non-averaging).

The re-sampling uncertainty, $\delta c_{ice,resampling}$ is the maximum c_{ice} - minimum c_{ice} difference of a 3 x 3 pixel window. The re-sampling uncertainty is computed on re-sampled data.

The total uncertainty is the squared sum of the algorithm and the re-sampling uncertainty, i.e.

$$\delta c_{ice,total} = \sqrt{\delta c_{ice,algorithm}^2 + \delta c_{ice,resampling}^2} \quad (18)$$

3.6 Level-4 algorithms

The level-4 processing includes the land-spill-over correction and the flags algorithms.

Land-spill-over correction

Land-spill-over correction is following the procedure described in Markus and Cavalieri (2009).

The flags

The flags are following the convention from earlier CCI sea ice concentration data sets:

Position over land	1
Position over lake	2
c_{ice} is set to 0 by open water filter	4
c_{ice} is set to 0 by land-spill-over correction	8
The 2 m air temperature is over 5°C	16
The climatological open water mask is applied	128

4 STRATEGIES FOR AN IMPROVED 100% TIEPOINT DURING THE SUMMER MELT SEASON

As pointed out by Kern et al (2016 and 2020) current sea-ice concentration algorithms including OSISAF/SICCI ones struggle with Summer ice conditions for 2 opposing reasons:

1. Melt-ponds on the ice surface has the same microwave signature as open water (leads) and will thus be interpreted as water (underestimation of the ice concentration).
2. The microwave signature of the ice between the ponds is very difficult to establish and is typically underestimated leading to an overestimation of the ice concentration of this ice.

Even though the 2 effects are opposing, they cannot be assumed to cancel each other since they are quite independent. This leads to a significant increase in the uncertainty of the derived ice concentration by any ice concentration algorithm.

The method described below does not allow for reduced uncertainties in total ice concentration per se, but rather allows for a more accurate computation of the ice surface fraction, since the ambiguity between open water and melt ponds cannot be resolved by microwave sensors that do not penetrate into water.

This chapter thus describes a method to derive Summer tie-points that better represents the ice between the melt-ponds, but as far as possible without interference from the ponds.

4.1 Background

During the Summer period when the ice is melting the low frequency brightness temperature of the ice alone will be quite stable (see Figure 12). This means that the measured 6 GHz brightness temperature can be used as fairly robust measures of the ice surface fraction within the resolution cell assuming that the signature of open water and this stable signature of ice are both known.

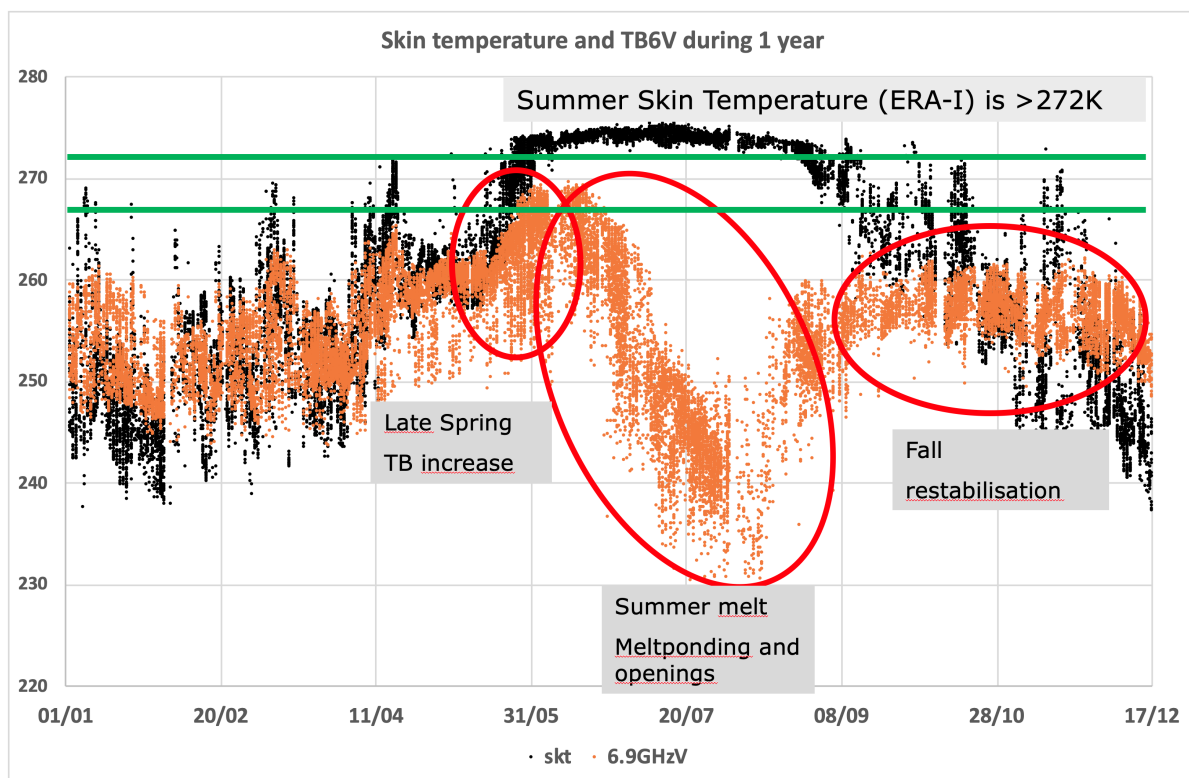


Figure 12: 6 GHz vertically polarised brightness temperature and ERA-Interim surface skin temperature time series from the high concentration dataset of the SIC Round Robin data base.

Figure 12 illustrates how the 6 GHz vertically polarised TB during May raises to a value close to 268 K as the surface skin temperature rises above the freezing point, and before melt ponds start to form.

Figure 13 further illustrates this as it shows a scatterplot of the close relationship between the 6 GHz TB and the ice surface fraction (ISF) (the fraction of the surface that is not water) derived from MODIS visible data. It is seen that the 6 GHz signature of water (ISF=0) can be well approximated by a constant value of 160 K.

This relationship allows us to derive the ISF from each individual 6 GHz vertically polarised TB measurement and subsequently derive ice signatures at other channels.

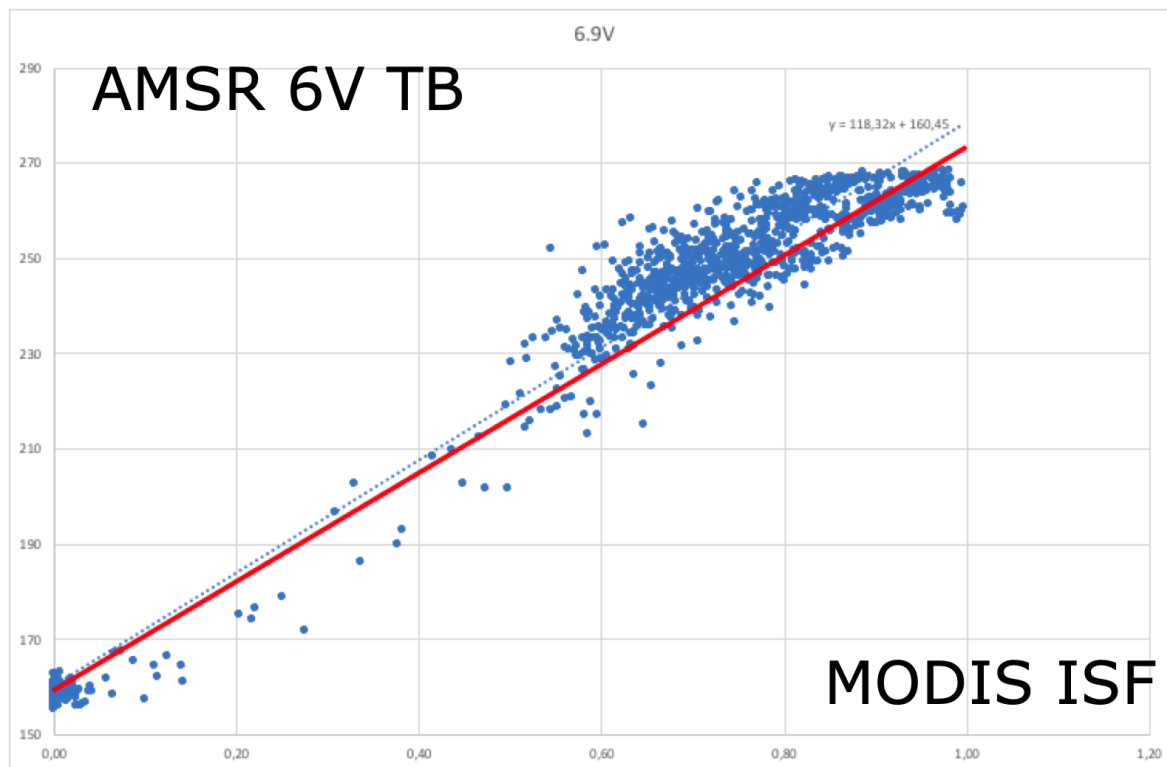


Figure 13: Scatterplot of 6 GHz vertically polarised TB vs MODIS Ice Surface Fraction (the fraction of the surface that is neither open water nor melt ponds). Data from the SIC Round Robin data base.

Given that we have simultaneous TB measurements at other frequencies and polarisations and that we also know the water signature at these channels (Table 3), the ice signature at these channels can now be estimated since the ISF is known.

Water		
Avg	Stdev	Channel
160.56	2.43	6.9V
79.88	4.06	6.9H
166.51	2.72	10.7V
85.82	5.43	10.7H
185.17	4.70	18.7V
110.03	9.91	18.7H
202.20	8.52	23.8V
137.98	16.76	23.8H
212.09	5.86	36.5V
147.32	13.76	36.5H
248.98	7.59	89.0V
207.74	19.78	89.0H

Table 3: List of water signatures at the 12 AMSR channels (from the open water SIC RRDB).

It is considered a reasonable assumption that the water signature at other channels can be considered constant since over the ice in the Arctic even during Summer the atmosphere is dry, and wind influence on surface roughness will be small due to the limited fetch of the leads and ponds.

4.2 Detailed method description

The basic assumption behind the algorithm is that at 6 GHz (Vertical polarization) during Summer ice has a stable brightness temperature (TB) of approximately 268K and water has another stable TB of approximately 160K (see section 4.1).

From these assumptions, the fraction of any pixel that is water respectively ice can be easily inferred from the 6V TBs actually measured.

$$TB_{6V} = ISF * TB_{6V}^{ice} + (1 - ISF) * TB_{6V}^{water}$$

$$ISF = \frac{(TB_{6V} - TB_{6V}^{water})}{(TB_{6V}^{ice} - TB_{6V}^{water})} \quad (19)$$

which is similar to e.g. the Comiso bootstrap ice concentration equation (Comiso, 1986, equation (5)).

ISF is ice surface fraction (the fraction of the surface that is ice/snow). (1-ISF) is the water surface fraction (leads+melt-ponds+other open water areas).

This ISF is valid at 6 GHz resolution, so subsequent use on other channels requires these to be resampled to 6 GHz resolution such as is available in AMSR-E L2A or AMSR2 L1R data.

Now assume that at any higher frequency we also have a good estimate of the TB of water (from e.g. the RRDP or the Dynamical TP process) we can now compute the TB of ice for any desired channel TB_x^{ice} in the measurement area (the desired channel at 6V resolution) from the observed TB(X) using the ISF from the 6V calculations above

$$TB_x = ISF * TB_x^{ice} + (1 - ISF) * TB_x^{water} \quad (20)$$

where X is the channel in question.

This can be solved to yield

$$TB_x^{ice} = \frac{TB_x - (1 - ISF)TB_x^{water}}{ISF} \quad (21)$$

This can in principle be computed for any pixel, irrespective of ice surface fraction larger than zero, but better accuracy (less noise) can of course be obtained from pixels with higher ISF.

Also, it is important for the above method that the resolution cells are the same at all frequencies, so a L1R type product is desired.

For TB(water) at the desired frequencies and polarisations, the SICCI2 AMSR-E and AMSR2 water TPs can be used or you can use the dynamically derived water tie-points from the normal dynamic TP method.

Note 1: The method above should only be applied during the period where TB(6V,ice) can be well approximated as 268K. This applies from approx. June 1 to early September. The exact period may be inferred from ERA5 2m air temperatures or surface skin temperatures larger than 272K. If available, a melt/freeze onset flag derived from the brightness temperature data themselves (e.g. Bliss and Anderson, 2018) can be used for guiding the derivation of the summer TP.

4.3 Example results

Figure 14 shows 18 GHz vertically polarised signatures of the ice between the ponds and leads derived using the method described in section 4.2. Note that during Winter and Spring the signatures are split in a high value for FY-ice and a lower value for MY-ice. From early June however, the signature collapses into one representing both ice types due to the melting at the surface. Late August the signature drops to that of winter MY-ice (at this stage all ice is per definition MY-ice) and gradually splits again as FY-ice starts to form.

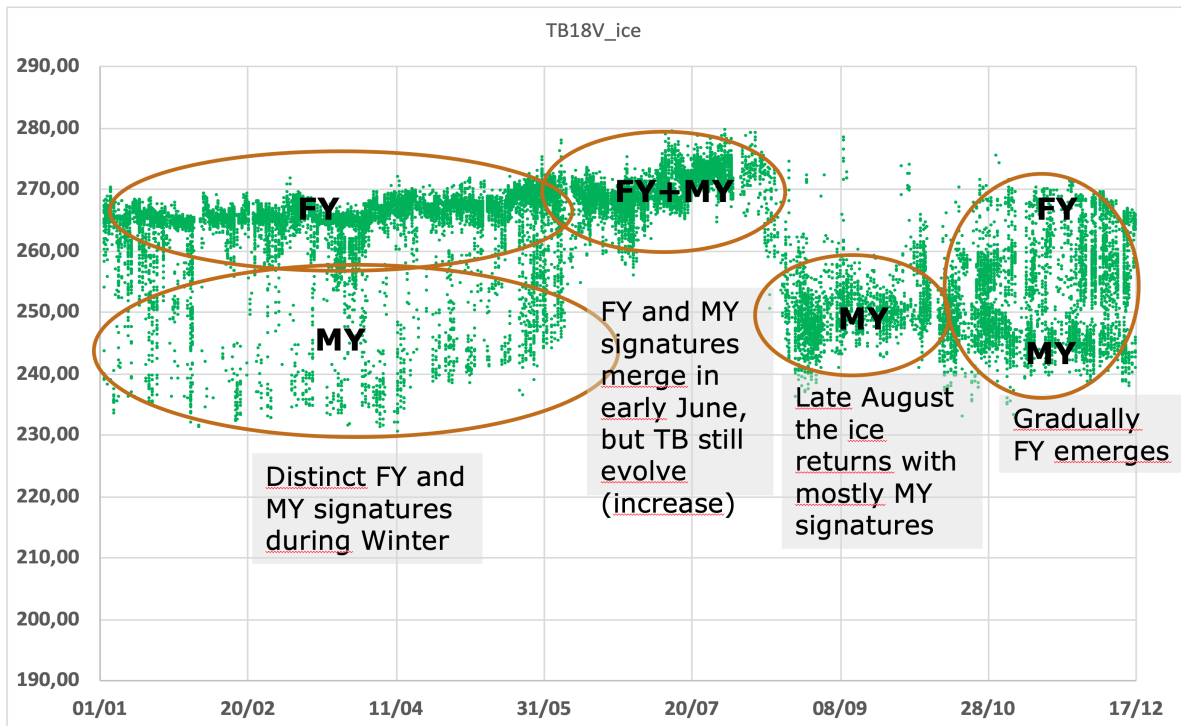


Figure 14: Time series of ice signatures at 18 GHz vertical polarisation derived using the proposed method.

Figure 15 illustrates how the application of the method provides significantly higher values of the sea ice signatures for two of the main channels in common SIC algorithms. The 37V plot in the lower left is similar to Figure 14 thus confirming that the method provides good results also at this higher frequency. To the right is a scatterplot of the new 18V and 37V sea ice signature TBs and a green line showing the standard 'ice line' employed by many ice concentration algorithms. The new 'ice line' lies significantly above the standard one explaining why the ice between the ponds and leads are typically overestimated by most algorithms. Note again that there is no way to distinguish open water in leads from melt-ponds at the ice surface, this would require the application of visible data such as Sentinel-3 OLCI.

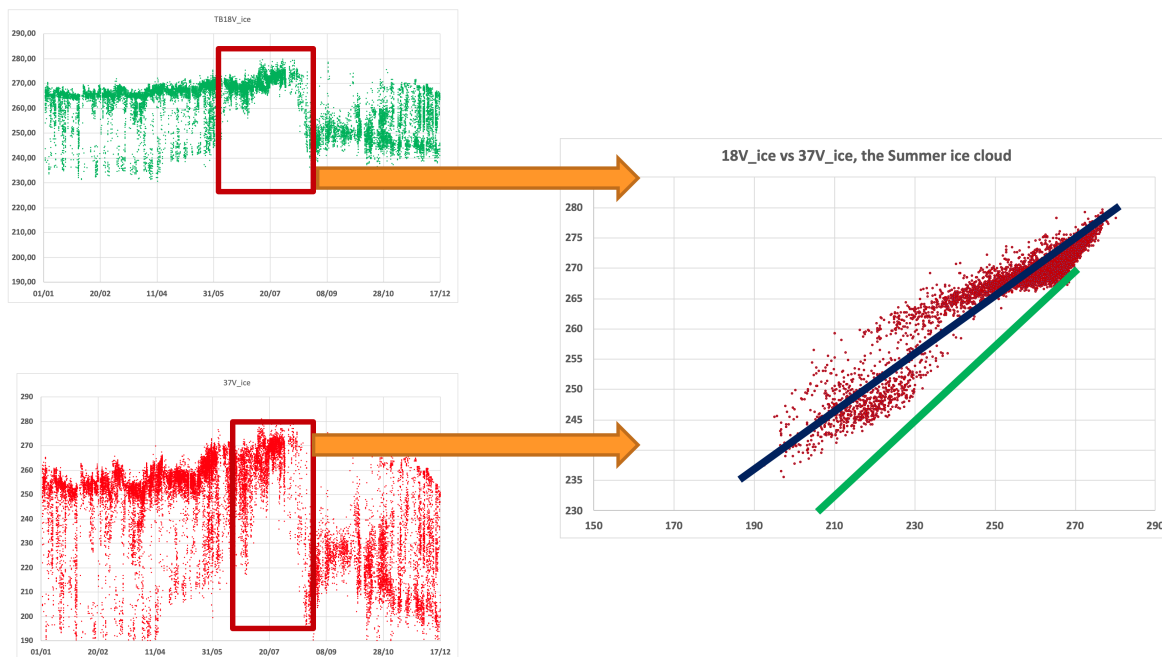


Figure 15: Upper left is a repeat of Figure 14 without the annotation, and lower left is a similar plot of the temporal evolution at 37 GHz vertical polarisation. To the left is the scatterplot of all data points within the red rectangle (the Summer period where the method is supposed to be valid). The green line shows the standard ice line normally used in many ice concentration algorithms and derived from Winter/Spring observations.

4.4 Step by step procedure for improved Summer ice TPs.

1. From May 15 to September 15, extract ERA-5 Tsk, TB6V and other TBs that are needed in the 'normal' Dynamical TP procedure. The TB data should be extracted from L1R data at 6 GHz resolution so all TB data have the same footprint.

2. Save TB data where $Tsk > 270K$ and e.g. NASATEAM SIC $> 80\%$.

3. For each sampled datapoint, calculate ISF as

$$ISF = (TB(6V) - TB(6V,water)) / (TB(6V,ice) - TB(6V,water))$$

where $TB(6V,water)=160K$ and $TB(6V,ice)=265K$.

Alternatively use the 6V, 37V, WS+Tsk algorithm developed in SICCI2 (requires extraction of both WS and Tsk from ERA-5 in step 1).

4. Correct each desired higher frequency TB to ISF=100% using

$$TB(X,100\% \text{ ice}) = (TB(X) - WSF*TB(X,water)) / ISF$$

5. The computed $TB(X, 100\% \text{ ice})$ constitute the Summer ice TP at channel X.

These Summer tie-points can now be used to calculate ISF using the algorithm of choice or can be fed into the algorithm using 'traditional' tie-points to estimate a bias between the standard (flawed) ice concentrations and the Summer ISF.

5 REFERENCES

Andersen, S., Tonboe, R., Kern, S., and Schyberg, H.: Improved retrieval of sea ice total concentration from spaceborne passive microwave observations using Numerical Weather Prediction model fields: An intercomparison of nine algorithms, *Remote Sens. Environ.*, 104, 374–392, 2006.

Andersen, S., Toudal Pedersen, L., Heygster, G., Tonboe, R., and Kaleschke, L.: Intercomparison of passive microwave sea ice concentration retrievals over the high concentration Arctic sea ice, *J. Geophys. Res.*, 112, C08004, <https://doi.org/10.1029/2006JC003543>, 2007.

Bliss, A. C., & Anderson, M. R.: Arctic sea ice melt onset timing from passive microwave-based and surface air temperature-based methods. *Journal of Geophysical Research: Atmospheres*, 123, 9063–9080. <https://doi.org/10.1029/2018JD028676>, 2018.

Cavalieri, D. J., Gloersen, P., and Campbell, W. J.: Determination of Sea Ice Parameters With the NIMBUS 7 SMMR, *J. Geophys. Res.*, 89, 5355–5369, 1984.

Cavalieri, D. J., Crawford, J., Drinkwater, M., Emery, W. J., Eppler, D. T., Farmer, L. D., Goodberlet, M., Jentz, R., Milman, A., Morris, C., Onstott, R., Schweiger, A., Shuchman, R., Steffen, K., Swift, C. T., Wackerman, C., and Weaver, R. L.: NASA sea ice validation program for the DMSP SSM/I: final report, NASA Technical Memorandum 104559, National Aeronautics and Space Administration, Washington, D.C., 126 pp., 1992.

Cavalieri, D. J., Parkinson, C. L., Gloersen, P., Comiso, J. C., and Zwally, H. J.: Deriving long-term time series of sea ice cover from satellite passive-microwave multisensor data sets, *J. Geophys. Res.*, 104, 15803–15814, <https://doi.org/10.1029/1999JC900081>, 1999.

Comiso, J. C.: Characteristics of arctic winter sea ice from satellite multispectral microwave observations, *J. Geophys. Res.*, 91, 975–994, 1986.

Donlon, C. J., Martin, M., Stark, J. D., Roberts-Jones, J., Fiedler, E., and Wimmer, W.: The Operational Sea Surface Temperature and Sea Ice analysis (OSTIA), *Remote Sens. Environ.*, 116, 140–158, <https://doi.org/10.1016/j.rse.2010.10.017>, 2012.

Gloersen, P., and F. T. Barath. A scanning multichannel microwave radiometer for Nimbus-G and SeaSat-A. *IEEE Journal of Oceanic Engineering OE-2(2)*, 172-178, 1977.

Gloersen, P., W. J. Campbell, D. J. Cavalieri, J. C. Comiso, C. L. Parkinson, H. J. Zwally. Arctic and Antarctic sea ice, 1978-1987: satellite passive-microwave observations and analysis. NASA SP-511, Washington D. C., 1992.

Hersbach, H., Bell, B., Berrisford, P., Hirahara, S., Horányi, A., Muñoz-Sabater, J., Nicolas, J., Peubey, C., Radu, R., Schepers, D., Simmons, A., Soci, C., Abdalla, S., Abellan, X., Balsamo, G., Bechtold, P., Biavati, G., Bidlot, J., Bonavita, M., De Chiara, G., Dahlgren, P.,

Dee, D., Diamantakis, M., Dragani, R., Flemming, J., Forbes, R., Fuentes, M., Geer, A., Haimberger, L., Healy, S., Hogan, R.J., Hólm, E., Janisková, M., Keeley, S., Laloyaux, P., Lopez, P., Lupu, C., Radnoti, G., de Rosnay, P., Rozum, I., Vamborg, F., Villaume, S. and Thépaut, J.-N. (2020), The ERA5 Global Reanalysis. *Q J R Meteorol Soc.* Accepted Author Manuscript. doi:10.1002/qj.3803

Hobbs, W., Massom, R., Stammerjohn, S., Reid, P., Williams, G., and Meier, W.: A review of recent changes in Southern Ocean sea ice, their drivers and forcings, *Global Planet. Change*, 143, 228–250, <https://doi.org/10.1016/j.gloplacha.2016.06.008>, 2016.

Ivanova, N., Pedersen, L. T., Tonboe, R. T., Kern, S., Heygster, G., Lavergne, T., Sørensen, A., Saldo, R., Dybkjær, G., Brucker, L., and Shokr, M.: Inter-comparison and evaluation of sea ice algorithms: towards further identification of challenges and optimal approach using passive microwave observations, *The Cryosphere*, 9, 1797–1817, <https://doi.org/10.5194/tc-9-1797-2015>, 2015.

Kern, S., Rösel, A., Pedersen, L. T., Ivanova, N., Saldo, R., and Tonboe, R. T.: The impact of melt ponds on summertime microwave brightness temperatures and sea-ice concentrations, *The Cryosphere*, 10, 2217–2239, <https://doi.org/10.5194/tc-10-2217-2016>, 2016.

Kern, S., Lavergne, T., Notz, D., Pedersen, L. T., Tonboe, R. T., Saldo, R., and Sørensen, A. M.: Satellite passive microwave sea-ice concentration data set intercomparison: closed ice and ship-based observations, *The Cryosphere*, 13, 3261–3307, <https://doi.org/10.5194/tc-13-3261-2019>, 2019.

Kern, S., Lavergne, T., Notz, D., Pedersen, L. T., and Tonboe, R.: Satellite passive microwave sea-ice concentration data set inter-comparison for Arctic summer conditions, *The Cryosphere*, 14, 2469–2493, <https://doi.org/10.5194/tc-14-2469-2020>, 2020.

Kilic, L., Prigent, C., Aires, F., Heygster, G., Pellet, V. and Jimenez, C.: Ice Concentration Retrieval from the Analysis of Microwaves: A New Methodology Designed for the Copernicus Imaging Microwave Radiometer, *Remote Sensing*, 12(7), 1060, doi:10.3390/rs12071060, 2020.

Kwok, R.: Sea ice concentration estimates from satellite passive microwave radiometry and openings from SAR ice motion, *Geophys. Res. Lett.*, 29, 1311, <https://doi.org/10.1029/2002GL014787>, 2002.

Lavergne, T., Sørensen, A. M., Kern, S., Tonboe, R., Notz, D., Aaboe, S., Bell, L., Dybkjær, G., Eastwood, S., Gabarro, C., Heygster, G., Killie, M. A., Brandt Kreiner, M., Lavelle, J., Saldo, R., Sandven, S., and Pedersen, L. T.: Version 2 of the EUMETSAT OSI SAF and ESA CCI sea-ice concentration climate data records, *The Cryosphere*, 13, 49–78, <https://doi.org/10.5194/tc-13-49-2019>, 2019.

Lu, J., Heygster, G., and Spreen, G.: Atmospheric Correction of Sea Ice Concentration Retrieval for 89 GHz AMSR-E Observations, *IEEE J-STARS.*, 11, 1442–1457, <https://doi.org/10.1109/JSTARS.2018.2805193>, 2018.

Ludwig, V., Spreen, G., Haas, C., Istomina, L., Kauker, F., and Murashkin, D.: The 2018

- North Greenland polynya observed by a newly introduced merged optical and passive microwave sea-ice concentration dataset, *The Cryosphere*, 13, 2051–2073, <https://doi.org/10.5194/tc-13-2051-2019>, 2019.
- Maass, N. and Kaleschke, L. Improving passive microwave sea ice concentration algorithms for coastal areas: applications to the Baltic Sea, *Tellus A*, 62, 393–410, <https://doi.org/10.1111/j.1600-0870.2010.00452.x>, 2010.
- Markus, T., D. J. Cavalieri. The AMSR-E NT2 sea ice concentration algorithms: its basis and implementation. *Journal of the Remote Sensing Society of Japan* 29(1), 216-225, 2009.
- Mäkynen, M. Sea ice concentration noise reduction using brightness temperature correction. EUMETSAT OSISAF visiting scientist activity report OSI_VS19_06, pp. 64. 2020.
- Meng, X.; Shen, H.; Li, H.; Zhang, L.; Fu, R. Review of the pansharpening methods for remote sensing images based on the idea of meta-analysis: Practical discussion and challenges. *Inform. Fusion*. 46, 102–113, 2019.
- Meier, W., Fetterer, F., Savoie, M., Mallory, S., Duerr, R., and Stroeve, J.: NOAA/NSIDC Climate Data Record of Passive Microwave Sea Ice Concentration, Version 3, NSIDC: National Snow and Ice Data Center, Boulder, Colorado, USA, <https://doi.org/10.7265/N59P2ZTG>, 2017.
- Parkinson, C. L., J. C. Comiso, H. J. Zwally, D. J. Cavalieri, P. Gloersen, W. J. Campbell (1987). Arctic sea ice, 1973-1976: satellite passive-microwave observations. NASA special publications.
- Peng, G., W. N. Meier, D. Scott, and M. Savoie. 2013. A long-term and reproducible passive microwave sea ice concentration data record for climate studies and monitoring, *Earth Syst. Sci. Data*. 5. 311-318. <https://doi.org/10.5194/essd-5-311-2013>
- Sabatini, R. R. (1972). THE NIMBUS 5 USER'S GUIDE, NASA Goddard Space Flight Center, NASA CR 139019, pp. 169.
- Sievers, I., J. A. Dawson, A. S. Jensen. Analysing Electrically Scanning Microwave Radiometer Data from the Nimbus-5 Mission. DTU Space pp. 43, 2020.
- Smith, D. M.: Extraction of winter total sea ice concentration in the Greenland and Barents Seas from SSM/I data, *Int. J. Remote Sens.*, 17, 2625–2646, 1996.
- Smith, D. M. and Barrett, E. C.: Satellite mapping and monitoring of sea ice, CB/RAE/9/2/4/2034/113/ARE, RSU, University of Bristol, Bristol, UK, 1994.
- Svendsen, E., Maetzler, C., and Grenfell, T. C.: A model for retrieving total sea ice concentration from spaceborne dual-polarized passive microwave instrument operating near 90 Ghz. *Int. J. Rem. Sens.* 8, no. 10:1479–1487, 1987.
- Tonboe, R. T., Eastwood, S., Lavergne, T., Sørensen, A. M., Rathmann, N., Dybkjær, G., Pedersen, L. T., Høyer, J. L., and Kern, S.: The EUMETSAT sea ice concentration climate data record, *The Cryosphere*, 10, 2275–2290, <https://doi.org/10.5194/tc-10-2275-2016>, 2016.
- Veng, T. Mapping of sea ice using NIMBUS 5 ESMR satellite data. Master thesis. DTU

Space. pp 39, 2021.

Wentz, F. J.: A model function for ocean microwave brightness temperatures, *J. Geophys. Res.*, 88, 1892–1908, <https://doi.org/10.1029/JC088iC03p01892>, 1983.

Wentz, F. J.: A well-calibrated ocean algorithm for SSM/I, *J. Geophys. Res.*, 102, 8703–8718, <https://doi.org/10.1029/96JC01751>, 1997.

Wentz, F. J. and Meissner, T.: AMSR ocean algorithm version 2, RSS Tech, Proposal 121599A-1, Remote Sensing Systems, Santa Rosa, California, 2000.